Three-dimensional mapping of mineral in intact shark centra with energy dispersive x-ray diffraction

J.-S. Park[1], H. Chen[2], K.C. James[3], L.J. Natanson[4], S.R. Stock[5,*]

[1] The Advanced Photon Source, Argonne National Laboratory, Lemont, IL
[2] Mineral Physics Inst., Stony Brook Univ., Stony Brook, NY
[3] Southwest Fisheries Science Center, National Marine Fisheries Service, NOAA, La Jolla, CA
[4] (retired) Northeast Fisheries Science Center, National Marine Fisheries Service, NOAA, Narragansett, RI
[5] Dept. of Cell and Developmental Biology, Feinberg School of Medicine and Simpson Querrey Inst., Northwestern University, Chicago, IL

* Corresponding author:
Mail address: as above 303 E. Chicago Ave., 60611-3008
E-mail address: s-stock@northwestern.edu

Co-author e-mail addresses:
JSP parkjs@aps.anl.gov
HC haiyan.chen@stonybrook.edu
KCJ kelsey.james@noaa.gov
LJN mangrules@yahoo.ca

Abstract:	271	words
Text:	7,774	words
Figures:	7	
Tables:	2	
References:	45	

Running title: 3D energy dispersive diffraction mapping of mineral in shark centra

Disclosures: The authors have no conflicts of interest.

Abstract

The centra of shark vertebrae consist of cartilage mineralized by a bioapatite similar to bone's carbonated hydroxyapatite, and, without a repair mechanism analogous to remodeling in bone, these structures still survive millions of cycles of high-strain loading. The main structures of the centrum are an hourglass-shaped double cone and the intermedialia which supports the cones. Little is known about the nanostructure of shark centra, specifically the relationship between bioapatite and cartilage fibers, and this study uses energy dispersive diffraction (EDD) with polychromatic synchrotron x-radiation to study the spatial organization of the mineral phase and its crystallographic texture. The unique energy-sensitive detector array at beamline 6-BM-B, the Advanced Photon Source, enables EDD to quantify the texture within each sampling volume with one exposure while constructing 3D maps via specimen translation across the sampling volume. This study maps a centrum from two shark orders, a carcharhiniform and a lamniform, with different intermedialia structures. In the blue shark (*Prionace glauca*, Carcharhiniformes), the bioapatite's *c*-axes are oriented laterally within the centrum's cone walls but axially within the wide wedges of the intermedialia; the former is interpreted to resist lateral deformation, the latter to support axial loads. In the shortfin mako (*Isurus oxyrinchus*, Lamniformes), there is some tendency for *c*-axis variation with position, but the situation is unclear because one dimension of the sampling volume is considerably larger than the thickness and spacing of the intermedialia's radially-oriented lamellae. Because elastic modulus in collagen plus bioapatite mineralized tissues varies significantly with both volume fraction of bioapatite and crystallographic texture, the present 3D EDD-derived maps should inform future 3D numerical models of shark centra under applied load.

Keywords: energy dispersive diffraction; bioapatite (hydroxyapatite); shark; centrum; mineralized cartilage; crystallographic texture

Introduction

Elasmobranchii, which include sharks, rays and skates, have cartilaginous skeletons, and relatively little is known (either experimentally or numerically) about how their subcranial axial skeletons function under in vivo loads. The sharks studied by Natanson et al. (2018) (elasmobranch orders Carcharhiniformes and Lamniformes) possess more than 80 vertebrae (Fig. 1a), each with a mostly unmineralized neural arch and a mineralized centrum, and these sharks' abdominal centra carry the loads generated during swimming (Porter and Long 2010). When a shark swims, its tail beats from left to right, compressing first one side then the other side of each centrum (Fig. 1b), and the magnitude increases from the juncture of the thorax and abdomen toward the tail. The structure and mineralization of the carcharhiniform and lamniform centra enables shark vertebrae to survive enormous compressive strains of 3-8% (Porter et al. 2014) for millions of cycles of loading (Watanabe et al. 2012), despite the absence of a repair mechanism like remodeling in bone.

Shark centra have complex 3D structures affecting mechanical performance, and there are significant similarities and important differences between carcharhiniform and lamniform centra. The centra of both orders contain an hourglass-shaped double cone of mineralized cartilage (Fig. 1c) termed the corpus calcarea. A fluid filled inter-vertebral capsule lies between the cone walls of adjacent vertebrae. Within a single centrum, the rostral and caudal cone walls are supported by the mineralized intermedialia whose structure differs between the two orders (Fig. 1c). In Carcharhiniformes, the intermedialia consists of four thick wedges (Fig. 1d) with unmineralized (cartilage) gaps separating the wedges. In Lamniformes, two dozen or more, relatively thin, radially-oriented plates (lamellae) comprise the intermedialia (Fig. 1d); these lamellae may be distinct from each other or may combine and separate from their neighbors, e.g.

81 the one o'clock position of the left side of Fig. 1d and Morse et al. (2022). The lamellae are
82 grouped into four sectors separated by four gaps; two sectors are wider and contain more
83 lamellae than the other two sectors. In both carcharhiniforms and lamniforms, the cartilage of
84 one pair of gaps extends to form the neural arch and that of the other pair to form the hemal arch
85 (if present).

86 During swimming, both the left and right sides of shark abdominal centra experience an
87 alternating pattern of compression and tension. Some studies of the macroscopic patterns of
88 strain in the shark vertebral column have appeared (Porter and Long 2010; Porter et al. 2014,
89 Porter et al. 2016), but little is known about the 3D distributions of displacement or of strain
90 within the complex structure of a shark centrum. Experimental measurement of these 3D strains
91 under applied load is one way forward and is, in fact, an eventual goal of the authors, see the
92 preliminary report of Park et al (2022c). An alternative to understanding centrum function is 3D
93 numerical modeling which requires accurate geometrical and materials property inputs, and
94 obtaining some of this information is the focus of the present report. Beyond the centra
95 macrostructure (3D geometry at the ~50 μm and higher scales), mineral density, microstructure
96 (scales 1 μm and above) and nanostructure (scales 0.1 nm and higher) contribute to functionality.
97 These centra structural levels are not independent, and, before introducing the energy-dispersive
98 x-ray diffraction-based nanostructural studies of this paper, prior studies of centra macrostructure
99 and microstructure are reviewed.

100 Macrostructure of entire lamniform and carcharhiniform centra have been studied with
101 microComputed Tomography (microCT) with volume elements (voxels) > 15 μm, e.g. Geraghty
102 et al. (2012), Natanson et al. (2018) and Morse et al. (2022). The last study found mineral levels
103 in the cone wall were significantly greater than in the intermedialia. As elastic moduli increase

104 with increasing mineral content in collagen-based tissues (Currey 2002), such mineral content
105 variation in centra should be incorporated into qualitative and/or quantitative models of response
106 to applied loads. Microstructure in small blocks cut from centra have been studied with microCT
107 with voxels ~ 1 μm in size (Stock et al. 2022), these very limited data need to be supplemented
108 before they can reliably guide understanding of mechanical properties. Nanostructure also affects
109 properties, and the focus here is on the nanocrystals of the mineral phase and the crystallographic
110 orientation of the mineral within the cartilage matrix. Data on bone suggests that mineralized
111 tissues consisting of collagen reinforced by bioapatite often contain a mineral phase where
112 certain crystal axes are strongly oriented relative to anatomical axes of principal in vivo stresses,
113 i.e., contain crystallographic texture (Currey 2002), and that this texture is strong enough to
114 produce significant variation in elastic constant as a function of orientation (Guo 2001). Failure
115 to incorporate such elastic modulus variation, if present in shark centra, into interpretation of
116 mechanical tests or in 3D modeling of shark centra may lead to inaccurate conclusions. Although
117 microstructural, micromechanical and histological studies have appeared on the mineralized
118 cartilage of shark tesserae, e.g. Chaumel et al. (2020) and Seidel et al. (2019, 2021), which is a
119 rather different tissue from that of the centra, crystallographic data are sparse for tesserae. Some
120 data, however, are available on shark bioapatite.
121 An early diffraction study (Urist 1961) showed that the centra's mineral is a bioapatite
122 closely related to hydroxyapatite (hAp), and TEM showed a similar bioapatite in shark tesserae
123 (Dean et al. 2005). Recently Park et al. (2022a) used monochromatic synchrotron x-radiation to
124 collect diffraction patterns from small blocks cut from centra of four species and confirmed that
125 the only crystalline phase visible was a bioapatite with lattice parameters slightly different from
126 those of bone and stronger crystallographic texture than in mammalian long bones. This latter

study, however, was not designed to compare texture from different portions of the centra, and 3D mapping of centrum texture is the focus of the present study.

The present authors hypothesize that, like the collagen fibril (type I collagen) and bioapatite orientations in long bones, the cartilage (2/3 collagen type II, 1/3 collagen type I plus significant proteoglycans) fiber axes and bioapatite crystal *c*-axes in shark centra are aligned along the direction(s) of principal strain and that these directions may vary with position within the centrum. The study reported below, performed at beamline 6-BM-B of the Advanced Photon Source (APS), employs energy dispersive x-ray diffraction (EDD) and a unique array of energy sensitive detectors (Weidner et al. 2010) to obtain 3D position resolved diffraction maps of two shark centra. The maps are obtained by X, Y and Z translation of the specimen across the sampling volume and without sample rotation. Alternative EDD data collection strategies have been used in the past, e.g. to study cement paste degradation due to sulfate attack (Naik et al. 2006) and to study the cross-section of bones (Stock et al. 2017), but the present instrument allows direct quantification of the 3D variation of crystallographic quantities (intensity of diffraction peaks, lattice parameters, crystallite size/microstrain, texture) within specimens. Alternative 3D diffraction mapping methods using monochromatic x-ray are available and are contrasted with this EDD approach in the Discussion.

This paper reports 3D EDD-derived maps of a carcharhiniform shark and a lamniform shark. Maps of mineral content are already available for intact centra (Morse et al. 2022), and the focus here is on crystallographic texture, something the authors expect will be essential to accurate 3D numerical modeling. Incorporation of texture and of mineral content into 3D models is also discussed.

Materials and Methods

One abdominal vertebrae of a species of Carcharhiniformes (*Prionace glauca*, blue shark, from vertebra numbers 81-84) and one of a species of Lamniformes (*Isurus oxyrinchus*, shortfin mako, vertebra number 62) were examined in this study. Laboratory microCT (Morse et al. 2022) showed the diameter and height were diameter 24.3 mm and 12.7 mm, respectively, for the blue shark centrum and 21 mm and 12.4 mm, respectively, for the shortfin mako centrum. Figure 1c shows 3D schematics of the two types of centra with the material closest to the viewer rendered transparent so the inner structure could be seen. Figure 1d shows transverse sections through the axial midplane of each centrum with the mineralized tissue shown in black.

The experimental geometry for EDD at beamline 6-BM-B, APS, is shown in Fig. 2a (Weidner et al. 2010). A collimator forms a pencil beam of polychromatic radiation which passes through the specimen (a schematic transverse section near the middle of a shortfin mako centrum). The conical receiving slits block all radiation except that diffracted from the sampling volume "sv" at an angle $2\theta = 6.5°$. Linear translators move the sample across the sampling volume along the three orthogonal axes X (horizontal, perpendicular to the incident beam), Y (vertical, perpendicular to the incident beam) and Z (horizontal, parallel to the incident beam).

Bragg's law, $\lambda = 2\, d_{hk.l} \sin\theta$, gives the angle θ at which peaks of diffracted intensity occur from crystalline material and shows that this angle depends on the x-ray wavelength (i.e., the inverse of the x-ray energy) and the crystal periodicity or d-spacing $d_{hk.l}$ for lattice planes *hk.l*.[1] With the Bragg angle fixed ($2\theta = 6.5°$), a range of energies in the polychromatic beam and an array of differently oriented crystals with the sampling volume sv, different *hk.l* select different energies and produce diffracted beams which reach one of the ten energy sensitive

[1] Here the abbreviated Miller-Bravais indexing system is used to emphasize the hexagonal crystal system of hAp (Cullity and Stock 2001).

172 detectors of the 6-BM-B array (Fig. 2b). For the bioapatite in the shark centra, each detector
173 measures the intensity of 00.2 diffraction of ~32 keV x-rays as well as the intensity of the
174 unresolved quadruplet of 21.1, 11.2, 30.0 and 20.2 of 38-42 keV x-rays and other reflections that
175 might be intense enough to pick out from the background. Note that the orientation of the
176 crystals diffracting into detector 5 is given by orientation of lattice plane normal $\mathbf{N}_5$ which makes
177 an angle $(90 - \theta)°$ from both the incident beam $\mathbf{S}_0$ and the diffracted beam direction $\mathbf{S}_5$ and which
178 lies in the horizontal plane (Fig. 2b). The same is true each other detector, i.e., for detector 1,
179 normal $\mathbf{N}_1$, $\mathbf{S}_0$ and the diffracted beam direction $\mathbf{S}_1$ are coplanar (vertical plane) and make the
180 same angles. Therefore, comparison of 00.2 diffracted intensities between different detectors
181 gives the relative fractions of crystalline bioapatite with different orientation defined by their
182 lattice normal orientations $\mathbf{N}_i$, i.e., the crystallographic texture within the sampling volume sv.
183 Figure 2c shows two views of the shortfin mako centrum (the side view in the top panel
184 and the central transverse section in the bottom panel). Figure 2d shows the same views of the
185 blue shark centrum. The red squares indicate extent of the specimen covered by the sampling
186 volumes; note that neither the spacing between sampling volumes nor their dimensions are to
187 scale.
188 Table 1 gives the experimental parameters for the scans of the two sharks. For the blue
189 shark and shortfin mako, the pencil beam dimensions were $\delta X = 0.1$ mm and $\delta Y = 0.2$ mm and
190 $\delta X = \delta Y = 0.2$ mm, respectively. A ~0.9 mm thick powdered ceria standard (NIST SRM 674B)
191 was scanned across the sampling volume, and the full-width at half-maximum of the diffracted
192 peak intensities was used as the measure of the gage length δZ along the incident beam direction.
193 The gage lengths for the different detectors varied slightly (see Supplemental Fig. S1, mean of
194 ~1.7 ± 0.15 mm) and sampled the same position within ~0.25 mm; these uncertainties are much

195 smaller than those from other sources and are hereafter ignored. For the beam dimensions used
196 to map the blue shark centrum, δZ averaged 1.7 mm, and for the shortfin mako, δZ averaged 2.5
197 mm. The translation step sizes used to build up the 3D maps were ΔX = 2.0 mm, ΔY = 1.0 mm
198 and ΔZ = 1.9 mm for the blue shark centrum and were ΔX = 1.5 mm, ΔY = 0.5 mm and ΔZ = 1.0
199 mm for the shortfin mako. Note that the entire volume of the blue shark centrum was scanned
200 (diameter 24.3 mm, height 12.7 mm), but only a portion of the shortfin mako centrum (diameter
201 ~21 mm, height 12.4 mm) was covered. For both centra, the 3D reconstruction on a 0.5 mm x 0.5
202 mm x 0.5 mm grid with interpolation of the neighboring volume elements (voxels) with
203 smoothing.

204 As noted in the previous paragraph, data collection parameters (and fraction of centrum
205 covered) differed for the two centra. Point by point mapping of 3D volumes is quite time
206 consuming: Ignoring motion and detector readout overhead, collecting the 16x10x17 = 2,720
207 patterns covering the blue shark centrum required 22.7 hr, and collecting the 3x10x47 = 1,410
208 patterns covering a portion of the shortfin mako centrum required 19.6 hrs. Limited beam time
209 (typically 4 days per scheduling cycle) dictated, therefore, that the sampling parameters were
210 altered match centra characteristics while not exhausting available time. Given the blue shark
211 intermedialia consisted of wedges, a relatively unform sampling grid was selected at the cost of
212 spatial resolution. Because the mako's intermedialia consisted of relatively thin lamellae
213 compared to the sampling volume dimension along the incident beam direction Z, sampling
214 along the beam direction was increased substantially compared to the blue shark, thereby
215 improving the chances that individual lamellae could be resolved, at the cost of decreasing the
216 volume scanned along X and Y.

The energy range of each detector was simultaneously calibrated using an array of ten, pre-aligned ^{57}Co sources. As mentioned above, a ceria standard was used to measure the sampling volume length along the beam direction. The *d*-spacings of the known ceria diffraction peaks were also used to confirm the linearity of the energy range.

The integrated intensity and position for each peak (00.2 and q) were determined by fitting a pseudoVoigt function (custom Matlab scripts). For each point-wise data set, integrated peak intensity for each peak (measured by each detector element in the detector array) was interpolated and smoothed using a 0.5 mm × 0.5 mm × 0.5 mm grid using Matlab *scatteredInterpolant* function with default parameters. The interpolated 3D maps were imported into ImageJ as a stack of slices and viewed with the orthogonal views function. Intensity maps from different detectors were combined using the color/merge function of ImageJ.

Results

Figure 3 shows a diffraction pattern (intensity vs x-ray energy) typical of a shark centra. Calibration lines from radioactive sources appear at high and low energies and are labeled "cal". Two bioapatite reflections are labeled 00.2 and "q", i.e., the closely spaced and unresolved quadruplet of 21.1, 11.2, 30.0 and 20.2. In Fig. 3, the maximum 00.2 and q peak intensities were ~150 cts and ~430 cts above background, respectively (compared to backgrounds of ~100 cts and ~120 cts, respectively). Two sections of the pattern are plotted in red; this is the energy range over which the 00.2 and quadruplet integrated intensities are calculated. The green peaks below the experimental data show peaks expected for a synthetic hAp reference pattern (Powder Diffraction File 86-1201, International Centre for Diffraction Data, Newtown, PA, USA), and there is a clear difference of in energy diffracted by each *hk.l* (the green peak reference position

vs red highlighted experimental data from a centrum), and, hence, a small but significant difference in lattice parameters. The ratio of 00.2 to q peak intensities in Fig. 3 is 35%, somewhat lower than the 45% ratio expected for the crystallographic-texture-free powder of PDF 86-1201.

Blue shark

Figure 4 shows orthogonal sections through the 3D reconstructed volume of the blue shark centrum using the integrated intensity of reflection q (unresolved 21.1+11.2+03.0+20.2). Within each panel, the three sub-panels show orthogonal sections, the square sub-panels being the transverse section through the axial center of the centrum and the yellow lines and arrows indicating the sections' positions in the 3D volume. In the top row, the left panel (labeled 5) is the reconstruction using intensities from detector 5), and the middle panel is intensities from detector 10, diametrically opposite detector 5. The right panel of the top row of Fig. 4 shows a composite of the two reconstructions with detector 5 intensities shown in blue and detector 10 intensities shown in red. The reconstructed transverse cross-sections look like the lab microCT reconstruction in Fig. 1d, if one allows for the lower spatial resolution of the EDD data.

The left panel of the bottom row of Fig. 4 plots intensities from detector 1, the middle panel plots intensities of detector 9 (diametrically opposite detector 1) and the right panel shows a composite with detector 1 intensity shown in red and detector 9 in blue. Although there are regions of red in the 1+9 composite panels, most of the volume appears magenta, i.e., more or less even intensities of the two opposite orientation detectors. In the composite 5+10, most of the volume is magenta but the regions of red intensity are more prominent at the margins of the mineralized tissue.

264 At some positions in longitudinal sections (those parallel to the centrum's axis and
265 running horizontally in Fig. 4), the integrated intensity of the q reflection is greater than in the
266 neighboring volume (yellow arrowheads); the higher intensity corresponds to the location of the
267 cone walls and the lower to intermedialia (Morse et al. 2022). In other portions of the same
268 sections, there is little difference in q intensity across the section (orange arrowheads). Table 2
269 gives values of the mean integrated intensity (and its standard deviation given after the ±
270 symbol) within the 3 x 3 voxel boxes within the cone wall and intermedialia. Inspection reveals
271 that the intensities vary within the intermedialia, and boxes *i* and *i'* were measured and show
272 ~50% variation (Table 2).
273 Crystallographic texture in mineralized tissues containing bioapatite typically manifests
274 in differences in 00.2 diffracted intensity along different anatomical directions. Figure 5, also of
275 the blue shark centrum, shows three orthogonal sections through the 00.2 intensity reconstructed
276 volume. In Fig. 5a, diffracted intensity from detector 5 is shown in blue, that from detector 7 in
277 green and that from detector 9 in red. The colored arrows in each panel indicate the direction of
278 *c*-axis crystallites sampled by the respective detector. Before describing what the different colors
279 within the sections reveal, it is useful to consider the magnitude of the integrated intensities
280 (Table 2). The largest integrated intensity within this 00.2-reconstructed volume is 86 arbitrary
281 units (a.u.) and the mean value within a 3 x 3 voxel box within fluid ("f" in Fig. 5a) is 2 a.u.
282 Within the sampling box in the cone wall, the mean 00.2 integrated intensity was 46 ± 9 a.u. for
283 detector 5 and 21 ± 5 a.u. for detector 1 (the direction equivalent to the detector 9 data plotted).
284 Within the sampling box in the intermedialia, the detector 5 intensity is 5 ± 1 a.u. and detector 1
285 intensity is 35 ± 2 a.u.

The transverse section through the middle of the centrum (the square image, lower left panel of Fig. 5a) has an intensity distribution like the transverse section shown in Fig. 1d, and, over most of the cross-section, the crystallites have *c*-axes oriented axially (red color indicating bioapatite *c*-axes primarily normal to the transverse plane, see coordinate axes at the lower left of this panel). In the side-view cross-section (upper panel of Fig. 5a) the blue voxels represent hAp crystallites with their *c*-axes oriented to diffract along the X direction (blue arrow), i.e., laterally (radially) in relation to the backbone axis, and the red voxels show crystallites with *c*-axes aligned axially. In the section of the right-hand panel of Fig. 5a, little blue appears; in this section blue indicates *c*-axis orientations out of the plane of this section and along the hoop (circumferential) direction; therefore, indicating large fractions of the hAp crystallites in the cone wall are not correctly oriented to diffract in the directions viewed by the respective detectors. Figure 5b schematically indicates observations shown in Fig. 5a: lateral (radial) *c*-axis orientations in the cone walls and axial orientations in the wedge between the cone walls (intermedialia).

Shortfin mako

Figure 6 shows reconstructed transverse sections (diffracted intensity vs position) for all ten detectors; maps for reflection q appear in (a) and for 00.2 appear in (b). A segmented lab microCT section of the mako centrum, at approximately the same axial position as the EDD maps and with the same orientation, is inset in the middle of the detector images in Fig. 6a. Gaps g1 and g2 between sectors can be resolved in all of the EDD maps and can be matched to g1 and g2 in the lab microCT-derived image. A small part of a wide sector s1, which borders gap g1, appears at the top of the maps in Fig. 6; the scan covers the outer ~3 mm of the radial lamellae.

309 A significant portion of sector s3 appears below gap g2, and each panel shows 4 mm of sector s2,
310 excluding the outer-most and inner-most portions of the lamellae.

311 The spatial distribution of q reflection intensities is the same for all of the detectors (Fig.
312 6a). The magnitude of intensities differs somewhat; they are greater for detectors 1-4 than for 6-9
313 and are larger for detector 5 than for the diametrically opposite detector 10. The sectors' borders
314 with the gaps have higher intensity than positions between the borders, consistent with the much
315 closer spacing of lamellae in these locations seen in microCT, i.e., the image in the center of Fig.
316 6a and in Morse et al. (2022). The intensity map of sector s2, for example, shows two radial
317 bands of increased intensity separated by a region of lower intensity. Away from its border with
318 the gap, the reconstructed portion of sector s3 contains three distinct bands radiating from the
319 middle of the centrum (indicated by the red arrows in the detector 8 map of Fig. 6a); the
320 intensities of these bands are substantially lower those bordering the gaps.

321 Outside of the centrum, the q intensity within the fluid is mostly below 100 a.u. although
322 there are scattered points where the measured intensity reaches 300 a.u. The maximum intensity
323 for this volume for all detectors is 1,200 a.u. Within s1, the intensities approach about 900 a.u.
324 for detector 1 and for 800 a.u. in detector 5. In the detector 1 map, the maximum intensities are
325 somewhat larger (~1,000 a.u.) within the 10 o'clock and 9 o'clock oriented radial lamella(e) of
326 s2 with the in-between volume having an intensity ~500 a.u. In the detector 5 map, the intensity
327 of the 10 o'clock lamella(e) is about 800 a.u. and somewhat larger than that in the 9 o'clock
328 band.

329 In many respects. the spatial distribution of 00.2 diffracted intensities mirrors that of the q
330 reflection maps. The radial bands bordering the gaps have higher intensities than sectors'
331 material between the gaps, but the three radial bands at the bottom of sector 3 are less clearly

defined for 00.2 than for q. The 00.2 intensities in the maps of detectors 4-6 are much greater than those collecting intensities at azimuths 90° away (detectors 1 and 2 and 8 and 9) and 180° away (detector 10). Further, the intensities in detector 1 and 2 maps are greater than those at corresponding positions in the 8 and 9 maps.

The maximum 00.2 integrated intensity for this volume for all detectors is 150 a.u., and the volumes containing only fluid (bottom area of the maps, below s3) are quite noisy intensity maps reflecting the especially poor counting statistics. Maximum intensity within the 10 o'clock orientated lamella(e) is about 90 a.u. in the detector 2 map and about 120 a.u in the 9 and 10 o'clock lamella(e) with lower intensities between the two. The base of the s3 band (right hand side of the map, 8 o'clock orientation) has an intensity of 60 a.u. for detector 3 whereas the intensity is 70 a.u. in the detector 5 map.

Discussion

There are at least two contexts where the EDD results reported above would be of interest to readers of a journal concerned with mechanical behavior. First, the successful EDD mapping in this paper is a precursor to 3D mapping of internal strains arising from in situ loading of shark centra. Second, the 3D mapping of various bioapatite characteristics (notably crystallographic texture) is essential input for accurate modeling. Before discussing the present EDD data and considering how these might apply in these two contexts, it is important to summarize what is known about the tissue most closely related to that of the shark centra, i.e., tessellated cartilage of sharks and related elasmobranchs, and to review prior mechanical behavior studies of centra.

Tessellated cartilage of sharks and related species related to centra tissue

357 To date, tessellated cartilage has received much more attention than the mineralized
358 cartilage of centra and, and these data may or may not guide understanding of centra mechanical
359 functionality. In polished sections of dry stingray tesserae, Seidel et al. (2019) found different
360 regions possess different mineral densities and nanoindentation hardnesses which they related to
361 mechanical functionality. Seidel at al. (2019) correlated tesserae mineral density with
362 nanoindentation hardness and found that stingray mineralized cartilage had a higher mineral
363 content than reported by Gupta et al. (2005) for calcified human cartilage, but the relationship of
364 Young's modulus to mineral content for tesserae was consistent with an extrapolation from data
365 for human calcified cartilage.
366 Elasmobranch tesserae contain chondrocyte lacunae and canaliculi, but most of their
367 volume is dense mineralized cartilage, at least at the one-micrometer level. In stingray tissue, for
368 example, the lacunae average 6-7 vol%, and the canaliculi may add an additional couple vol%
369 porosity (Chaumel et al. 2020). This tissue microstructure is quite different from that of shark
370 centra, e.g. Fig. 5 of Stock et al. (2022): from this image, the present authors estimate ~76 vol%
371 pores/soft tissue and 3-4.5 µm trabeculae thickness for the intermedialia volume and 59 vol%
372 pores/soft tissue and ~8 µm trabeculae thickness for the cone wall volume. Even if the
373 mineralized cartilage constitutive properties (mineral content, elastic moduli, yield stress,
374 fracture toughness, …) are the same at the 50-1,000 nm scale for both tissues, the very different
375 microarchitectures of tesserae and centra suggest very different mechanical properties at scales
376 one micrometer and above.
377
378 *Prior studies of centra mechanical behavior*

379 Before discussing prior studies of mechanical functionality of centra, it is useful to
380 consider what is known about the mechanical properties of tessellated tissue, the tissue most
381 closely related to that of centra. Liu et al. (2014) applied compressive loading normal to and
382 parallel to the plane of blue shark jaw tesserae surrounded by uncalcified cartilage; their focus
383 was measuring and modeling stress relaxation behavior during in vivo biting and their values of
384 elastic moduli are informative for the unmineralized cartilage but not for mineralized tesserae.
385 One way to isolate the calcified tissue is to produce polished sections of tesserae and perform
386 nanoindentation, and, depending on the position within stingray tesserae, the resulting Young's
387 moduli range from 15 to 35 GPa for tissue densities 1.5 to 2.7 g/cm^3, respectively (Seidel et al.
388 2019), which on average are higher than in human cortical bone (Guo 2001).
389 Porter and Long (2010) tested vertebrae (neural arch plus centrum, centrum alone) from a
390 carcharhiniform shark in uniaxial compression and determined that the arch did not carry
391 appreciable load. The experimental Young's modulus determined was ~150 MPa which
392 combines the tissue's intrinsic properties and deflection of the double cone and intermedialia
393 structure, i.e., the continuum structural modulus.
394 Porter et al. (2014) studied in vivo and in situ strains of dogfish vertebrae using
395 sonomicrometry. During low velocity swimming, compressive and tensile strains up to 2% were
396 observed; post mortem ex vivo experiments imposing curvatures seen in steadily swimming
397 dogfish revealed tensile strains approaching 4%. Ingle et al. (2018) performed cyclic
398 compressive testing on vertebrae from carcharhiniforms and lamniforms and found anterior
399 vertebrae had lower continuum moduli than posterior vertebrae; in all cases these moduli were
400 less than 10 MPa. In three-point bending, more closely approximating loading in vivo than
401 simple compression, Long et al. (2011) measured the apparent storage and loss moduli (E' and

E'', respectively) of segments of multiple shark vertebrae. Depending on the amplitude of maximum curvature, the elastic portion of the modulus E' was between 0.3 and 1.3 MPa, for a fast swimming carcharhiniform species and 0.1 and 0.6 MPa for a carcharhiniform species known less for its speed and more for its maneuverability.

Blue shark

Interpretation of EDD intensity maps from the carcharhiniform centrum (blue shark) is much more straightforward than for the lamniform centrum (shortfin mako). Most of the centrum volume outside of the double cones of carcharhiniforms is occupied by four wedges (Fig. 1) with uniform microstructure down to the 15-25 μm level over millimeter lengths (Morse et al. 2022). Cone walls are multiple EDD voxels thick. Away from the edges of the cone walls, therefore, changes in diffracted intensity (greater than random variation) must result from differences in crystallographic texture.

As shown in Fig. 5 of the blue shark, bioapatite *c*-axes within the cone walls are strongly aligned laterally (i.e., along radii from the axis of the centrum), and the *c*-axes within the intermedialia are aligned axially. If the variation elastic properties with texture of sharks' mineralized cartilage resembles those of bone, something reasonable to assume for bioapatite-collagen based natural composites, then the strong *c*-axis directionality in the blue shark centrum (Fig. 5) corresponds to directional differences in elastic constants. In the cortices of human long bones, for example, bioapatite *c*-axes tend to be oriented along the axis of the bone, and elastic moduli for longitudinal vs transverse anatomical orientations are 1.8x greater for the former than the latter (Guo 2001). Park et al. (2022a) showed sharper *c*-axis texture in tissue cut from shark centra (both lamniforms and carcharhiniforms) than is observed in bone, and we hypothesize that

425 spatial/directional variation of moduli may be more pronounced in the mineralized shark centra
426 than in long bones. If, like in bone, it is correct to infer increased stiffness along directions where
427 *c*-axes are concentrated, then it appears that the mineral in the carcharhiniform cone walls is
428 aligned to resist lateral deflections and that the mineral in the intermedialia is aligned to resist
429 axial compression. 3D numerical models could confirm or refute this conjecture by incorporating
430 elastic constants consistent with the 3D EDD maps with geometry derived from lab microCT of
431 centra.

432 In Fig. 4 (reflection q of the blue shark centrum), comparison of the intensity map of
433 detector 5 vs detector 1 (or 9) shows a difference of intensity only in the small sector oriented at
434 11 o-clock; however, the intensity map of the 11 o'clock section for detector 10 (diametrically
435 opposite of detector 5) does not differ from those of detectors 1 (or 9). On balance, reflection q
436 of the blue shark reveals weak texture, not unlike the weak texture seen for this set of reflections
437 in mineralized tissues based on a type I collagen matrix (bone, dentin, cementum) reinforced
438 with bioapatite, i.e., Almer and Stock (2005), Stock et al. (2014), Ryan et al (2020), Park et al.
439 (2022b).

440

441 *Shortfin mako*

442 The EDD maps of the shortfin mako centrum (Fig. 6) cover only part of the intermedialia
443 and none of the cone wall; because the lamellae were so narrow, this choice was made to obtain
444 highest spatial resolution in the available beam time. One cannot compare, therefore, the texture
445 of the cone walls with that of the lamellae for this data set. If the mako intermedialia texture
446 were the same as in the blue shark intermedialia, the 00.2 intensities of detectors 1 and 9 would
447 be substantially larger than those in detectors 5 and 10. The situation, however, appears more

448 complicated in the shortfin mako centrum: the 00.2 intensities of detector 5 and 9 are
449 comparable, that of detector 1 is the largest of all detectors and that of detector 10 is substantially
450 lower than any other detector. Note also that the detectors with an upward component (1-4) have
451 higher intensities than those with a downward component (6-9).

452 The reduced axial orientation in the intermedialia of the shortfin mako compared to that
453 of the blue shark tempts one to speculate that mechanical loading of the lamellae differs from
454 that of the wedges and that this drives the difference in *c*-axis orientation (and in the underlying
455 cartilage). Lamellae must resist out of plane bending produced by applied axial compression.
456 The situation is further complicated by the fact that lamellae experience reactionary axial tensile
457 loading when opposite side of the centrum is compressed. With multiaxial resistance required,
458 one would expect the *c*-axes of growing mineralized tissue to be laid down in more isotropic
459 orientations. In contrast, most of the wedge volume in carcharhiniforms has pronounced lateral
460 constraint from the surrounding material, and one would expect axial reinforcement is the main
461 requirement on the mineral phase. However attractive this speculation is, it needs to confirmed
462 by improved measurements.

463 For the shortfin mako centrum, the quadruplet reflections show some intensity variation
464 between maps with different detectors (Fig. 6). Like that seen in the 00.2 maps, detector 5
465 intensity is greater than detector 10. In Fig. 6, detectors 4-6 also have greater intensities than
466 detectors 1-3 and 7-9. The quadruplet reflection for the shortfin mako centrum, therefore, is more
467 revealing of texture than the same reflection in bone. This is not unexpected because the matrix
468 of shark centra is cartilage (and not type I collagen), and WAXS and SAXS of blocks of tissue
469 cut from centra showed organization of the bioapatite nanoparticles a bit different from that in
470 bone (Park et al. 2022a).

471 The authors anticipated that the relatively large sampling volume length along the beam
472 direction and the narrow width of the lamellae in the shortfin mako intermedialia (Fig. 1) would
473 complicate analysis and therefore concentrated available scanning time on sampling with a much
474 finer grid over a much smaller volume than in the blue shark. Despite this, interpretation of the
475 shortfin mako EDD data is still confounded by sub-voxel sampling: in some positions it appears
476 two, three or more lamellae contribute intensities and nearby voxels only one lamella
477 contributes. Three radial bands (red arrows at the bottom of Fig. 6a) are structures where
478 individual lamellae or pairs of lamellae are sampled whereas the bands bordering the gaps are
479 examples of signals from larger groups of lamellae combined in a single EDD voxel. As it is
480 unlikely that EDD mapping with isotropic 100 μm voxels will be achieved in the near future,
481 interpretation of data from lamniform centra will require care and be circumscribed with caveats
482 whereas analysis of carcharhiniform centra should be straightforward. Accurate registration of
483 lab microCT and EDD reconstructions could offer a way forward in studying lamniform
484 intermedialia, but implementing, validating and applying such methodologies is apt to be
485 extremely laborious.
486
487 *In situ EDD strain mapping of centra*
488 The studies cited above (Porter and Long 2010, Long et al. 2011, Porter et al. 2014, Ingle
489 et al. 2018) demonstrated shark centra experience large continuum level strains in vivo but did
490 not reveal (a) whether the mineral and not merely the type II cartilage was deforming nor (b)
491 whether, if the mineral phase does carry strain, this strain varies as a function of position. Stock
492 et al. (2022) used synchrotron microCT to show that cone walls and intermedialia consisted of
493 thin, closely-spaced trabeculae with a substantial volume fraction of unmineralized tissue.

494 Concerning question (a), Stock et al. (2021) found that a polymer matrix composite containing a
495 very large volume fraction of synthetic hAp particles and an open framework of struts
496 experienced large structural distortions (engineering strains > 20%) without hAp carrying
497 appreciable strain. Regarding question (b), Park et al. (2022c) presented a preliminary report of
498 EDD-derived strain maps in a shark centra under compression but did not report detailed
499 analyses.

500 Use of purpose-built load frames for tomography studying specimens under load, e.g.
501 Breunig et al. (1992, 1993), and position-resolved strain quantification under applied load for
502 mineralized tissues, e.g. Almer and Stock (2010), Stock et al. (2011), are not new, but the
503 approach of Park et al. (2022c) is novel because EDD is used and because these are the first
504 positioned resolved and in situ strain measurements for shark mineralized tissue. In this proof of
505 principle experiment, Park et al. used spacers within a plastic jar, between jar's lid and base, to
506 compress the centra by known increments. The sampling volume was scanned across the middle
507 transverse plane of the centra with no applied displacement and after one increment of
508 compression. Changes in diffraction peak positions for the detector pair 5 and 10 and for pair 1
509 and 9 are the basis for the strain determination, a standard x-ray diffraction approach, and Park et
510 al. (2022c) found shifts in bioapatite peak positions for different displacements, indicating the
511 mineral phase was being strained. Work remains before 3D maps of strain distributions are
512 extracted.

513

514 *Modeling of centra response to loading*

515 The authors are unaware of any 2D or 3D modeling of shark centra response to
516 deformation. Mineralized shark cartilage, however, has been modeled numerically for several

517 interconnected tesserae (Seidel et al. 2019). The tesserae modeling was 2D and considered two
518 structural units: stiffer, more highly-mineralized, radially-oriented spokes and inter-spoke
519 volumes. Synchrotron microCT of centra (Stock et al. 2022) indicates the micrometer-level
520 structure of centra is quite different from that of tesserae, so the results of Seidel et al. (2019) are
521 not directly transferrable to centra. MicroCT-based, 3D models of trabecular bone and of antler
522 are well developed, e.g., Kinney et al. (2000), Niebur et al. (2000), van Rietbergen (2001), Gupta
523 et al. (2013), and use of these approaches might be very valuable with centra.
524 Modeling shark centra is outside of the areas in which the authors work. However, the
525 available macrostructural, microstructural, mineral density and crystallographic texture data
526 suggest differences, particularly between cone and wedge, evolved to provide improved
527 mechanical functionality. The authors propose the following sequence of simple-to-complex
528 models (Fig. 7) as an effective approach. For purposes of illustration, the present discussion is
529 restricted to the more geometrically simple carcharhiniform centra (intermedialia consisting of a
530 pair of large medio-lateral wedges and a pair of dorsal-ventral wedges) and ignores lamniform
531 centra (intermedialia consisting of closely-spaced, diverging and merging lamellae), see Morse et
532 al. (2022).
533 A first step could be 2D simplifications based on the diametral section through the center
534 of medio-lateral wedges (locations at “xs” in the middle panels of Fig. 7a-c and sections shown
535 in the bottom panels of Fig. 7a-c). This section is the one that would experience the largest range
536 of in vivo strains. The simplest loading regime is uniaxial compression, applied load P, and
537 simplest centrum model consists of three materials (Fig. 7a): unmineralized cartilage “uc” of the
538 gap regions between wedges (“g” in Fig. 1), mineralized cartilage “mc” of the centrum (ignoring
539 differences in mineralization levels between cone and intermedialia) and intervertebral fluid

"ivf" (incompressible, sealed in the volume between cones of adjoining centra). In the 2D model, one could investigate the effect of mineralized cartilage's (isotropic) Young's modulus on strain distribution. Different hourglass angles α, centrum heights h and diameters ϕ occur along the length of the shark vertebral column and for different carcharhiniform species (Ingle et al. 2018, Morse et al. 2022), and the effect of these on strain distributions can also be examined parametrically. Simple uniaxial compression of the same three-component model can be extended to a distribution of loads representing in vivo bending (bottom panel, Fig. 7b).

The next level of complexity for a 2D model is partitioning the mineralized cartilage into cone "c" with thickness δ and intermedialia "i" with isotropic Young's moduli E_c and E_W, respectively. Although centra tissue moduli data do not presently exist, one expects $E_c > E_W$ because carcharhiniform cones contain more mineral than their intermedialia (Morse et al. 2022), and, as a zero-order approximation, one expects a relationship between tissue mineral level and Young's modulus similar to that in bone (Currey 2002). Different combinations of α, h, ϕ and δ could be examined virtually and compared to what nature has evolved.

Centra are 3D structures, and the 2D models would not be expected to capture all aspects of deformation. The 3D macrostructure can be imported into a finite element or other numerical model using 3D microCT data, e.g. Morse et al. (2022). As mentioned above, this approach is widely applied for trabecular bone, and a sampling of such studies can be found elsewhere (Stock 2019). Following the steps outlined above in 2D, a three-component, two-material system with isotropic Young's moduli would be modeled first in uniaxial compression (Fig. 7a, top) and then in bending (Fig. 7b, top). Note that $E_{mc} >> E_{uc}$, where mc and uc denotes the mineralized and unmineralized cartilage, respectively. One expects a slight variation in strains between the

562 the wedge interiors to the volumes bordering the gaps containing unmineralized cartilage. It
563 would also be interesting to see whether strain varied radially and axially within the wedge.
564 The next step might be partition of the mineralized tissue into cone and intermedialia
565 with isotropic Young's moduli $E_c > E_W$. In addition to the spatial variations mentioned in the
566 previous paragraph, strain gradients may occur between cone and intermedialia.
567 Based on the EDD observations reported above, namely, that strong bioapatite *c*-axis
568 crystallographic textures occur in the cone and intermedialia, the authors believe that accurate
569 modeling will require anisotropic moduli for both structures. In the centrum's coordinate system
570 of tangential, radial and axial directions, denoted *t*, *r* and *a*, respectively (Fig. 7d), the anisotropic
571 Young's moduli are denoted E_t, E_r and E_a, , respectively. More experimental work is required to
572 determine how much E_t, E_r and E_a actually differ, but this could be examined virtually via the 3D
573 model.
574
575
576 *Alternatives to EDD and future experiments*
577 Alternatives to EDD exist which are suitable for samples containing nanocrystals (such as
578 are present in bioapatites), which employ monochromatic x-radiation and which might allow
579 diffraction from an individual lamella to be isolated from that of closely spaced neighbors. Use
580 of conical slits (Park et al. 2013) or spiral slits (Martins et al. 2010) with monochromatic x-rays,
581 for example, allows diffraction patterns to be collected with a simple area detector and would not
582 require a specialized detector array. Translation similar to that employed here would allow 3D
583 reconstruction of the volume, but the sampling volume would be elongated along the beam
584 direction like that in the present study. Insertion devices such as that of 1-ID, APS, presently

offer orders of magnitude greater flux at any selected wavelength compared to 6-BM-B, and the greater flux could be traded for finer spatial sampling. Conical slits tailored for monochromatic x-rays and the hexagonal crystal system (i.e., for bioapatites) do not appear to exist, limiting the number of diffraction peaks which can be collected simultaneously, but spiral slits can capture all of the hexagonal reflections at the same time albeit with azimuthal gaps in the diffraction rings. It is, however, extremely difficult to obtain beam time at 1-ID, APS, so EDD at 6-BM-B, APS, remains an extremely attractive option.

An alternative to slit-based approaches is x-ray diffraction tomography with an incident monochromatic pencil beam, an open area detector and translation-rotation data acquisition, e.g. Stock et al. (2008), Birkbak et al. (2015). Reconstruction of cross-sectional variation of diffracted intensity employs back projection or other computed tomography algorithm. Compared to the translation-rotation method, 3D EDD mapping has the advantage of isolating diffraction from the sampling volume from all other scattering. Additionally, EDD mapping does not require specimen rotation, and specimens with complex surrounding tissue can be aligned so these structures do not affect the diffraction signal. For completeness, one should mention the 3D scattering approach termed tensor tomography which has been applied to bone, e.g. Maleki et al. (2014), but only to relatively small sections cut from larger specimens.

Accumulated x-ray damage affects mechanical properties of collagen-based mineralized tissues (Barth et al. 2011), these effects rise with increasing dose and become a concern in the context of in situ loading and strain measurements. While estimating dose is fairly straightforward with monochromatic high-energy x-rays, e.g., Stock et al. (2020), quantitative estimates for polychromatic x-radiation cannot currently be made mainly because incident x-ray spectra (intensity vs energy) are unavailable for the 6-BM-B bending magnet. Were the spectra

608 available, one could then calculate dose for each energy using tabulations such as that of Hubble
609 and Seltzer (2004) and sum the individual contributions.

610 In qualitative terms, 3D mapping with EDD damages the tissue much more than the
611 monochromatic, high-energy techniques described above; this may not be an issue for one-and-
612 done mapping (like the data reported above) but might be for in situ loading experiments. First,
613 photons in the 25-55 keV range (the EDD data) deposit much more energy per photon those at
614 70 keV and above. Second, in monochromatic methods, all of the photons traversing the
615 specimen have the potential to contribute to the diffracted signal whereas in EDD, photons with
616 energies between those diffracted into the detectors, deposit energy in the specimen and do not
617 contribute to signal. Third, all points along the path of the incident beam are exposed when
618 diffraction from one sampling volume is collected: If ten positions through the sample thickness
619 are sampled, then the dose is ten time larger over the entire thickness.

620 Some damage to mineralized tissue samples is inevitable for x-ray-based methods such as
621 diffraction, and damage is minimized if each sampled volume is exposed once for the minimum
622 time required to obtain useful signal. In diffraction quantification of internal strains
623 accompanying four-point bending, for example, Gallant et al. (2014) made use of the fact that the
624 tensile to compressive strain gradients are nominally the same for all cross-sections within the
625 inner span of the apparatus; they translated to a new cross-section before measuring strains for
626 each increment of deflection. This approach could be adapted for EDD mapping of the
627 intermedialia of carcharhiniform centra where strains should vary continuously. With reference
628 to Fig. 2d, one could collect data at the red squares' positions for one increment of deformation
629 and then at an adjacent position for the next.

630 The preliminary report of Park et al. (2022c) suggests in situ compression and EDD 3D
631 mapping of strains in the bioapatite phase of shark centra will be very informative in describing
632 how the centra function mechanically. It should be straightforward use EDD to apply x-ray
633 diffraction strain quantification under four-point bending (e.g. Gallant et al. 2014) to segments of
634 multiple shark vertebrae (e.g. Long et al. 2011), i.e., in a loading mode more closely
635 approximating that in vivo.
636
637 **Acknowledgements**
638 Beamline 6-BM-B, APS, is supported by COMPRES, the Consortium for Materials
639 Properties Research in Earth Sciences under NSF Cooperative Agreement EAR-1661511. This
640 research used resources of the Advanced Photon Source, a U.S. Department of Energy (DOE)
641 Office of Science User Facility, operated for the DOE Office of Science by Argonne National
642 Laboratory under Contract No. DE-AC02-06CH11357. Argonne National Laboratory's work was
643 supported by the U.S. Department of Energy, Office of Science, Office of Basic Energy
644 Sciences, under contract DE-AC02-06CH11357.
645
646 **References**
647
648 Almer, J.D., Stock, S.R. 2005. Internal strains and stresses measured in cortical bone via high-
649 energy x-ray diffraction. J Struct Biol **152**, 14-27.
650 Almer, J.D., Stock, S.R. 2010. Loading-related strain gradients spanning the mature bovine
651 dentinoenamel junction (DEJ): Quantification using high energy x-ray scattering. J Biomech
652 **43**, 2294-2300.

653 Barth, H.D., Zimmermann, E.A., Schaible, E., Tang, S.Y., Alliston, T., Ritchie, R.O. 2011.
654 Characterization of the effects of x-ray irradiation on the hierarchical structure and
655 mechanical properties of human cortical bone. Biomater **32**, 8892-8904.
656 Birkbak, M.E., Leemreize, H., Frølich, S., Stock, S.R., Birkedal, H. 2015. Diffraction Scattering
657 Computed Tomography: A Window into the Structures of Complex Nanomaterials.
658 Nanoscale **7**, 18402 – 18410.
659 Breunig, T.M., Stock, S.R., Antolovich, S.D., Kinney, J.H., Massey, W.N, Nichols, M.C. 1992.
660 A Framework Relating Macroscopic Measures and Physical Processes of Crack Closure of
661 Al-Li Alloy 2090. in *Fracture Mechanics: Twenty-Second Symposium (Volume 1)*, ASTM
662 STP **1131** (1992) 749-761.
663 Breunig, T.M., Stock, S.R., Brown, R.C. 1993. Simple Load Frame for in situ Computed
664 Tomography and X-ray Tomographic Microscopy. Mater Eval **51**, 596-600.
665 Chaumel, J., Schotte, M., Bizzarro, J.J., Zaslansky, P., Fratzl, P., Baum, D., Dean, M.N. 2020.
666 Co-aligned chondrocytes: Zonal morphological variation and structures arrangement of cell
667 lacunae in tessellated cartilage. Bone **134**, 115624.
668 Cullity, B.D., Stock, S.R. 2001. *Elements of X-ray Diffraction*, 3rd Ed., Prentice-Hall: Upper
669 Saddle River.
670 Currey, J.D. 2002. *Bones – Structure and Mechanics* Princeton: Princeton Univ. Press.Dean,
671 M.N., Chiou, W.-A., Summers, A.P. 2005. Morphology and ultrastructure of prismatic
672 calcified cartilage. Microsc Microanal **11**, 1196-1197.
673 Gallant, M.A., Brown, D.M., Hammond, M., Wallace, J.M., Du, J., Deymier-Black, A.C.,
674 Almer, J.D., Stock, S.R., Allen, M.R., Burr, D.B. 2014. Bone cell-independent benefits of

675 raloxifene on the skeleton: A novel mechanism for improving bone material properties.
676 Bone **61**, 191-200.
677 Geraghty, P.T., Jones, A.S., Stewart, J., Macbeth, W.G. 2012. Micro-computed tomography: an
678 alternative method for shark aging. J Fish Biol **80**, 1292-1299.
679 Gupta, H.S., Krauss, S., Kerschnitzki, M., Karunaratne, A., Dunlop, J.W.C., Barber, A.H.,
680 Boesecke, P., Funari, S.S., Fratzl, P. 2013. Intrafibrillar plasticity through mineral/collagen
681 sliding is the dominant mechanism for the extreme toughness of antler bone. J Mech Behav
682 Biomed Mater **28**, 366-382.
683 Gupta, H.S., Schratter, S., Tesch, W., Roschger, P., Berzlanovich, A., Schoeberl, T., Klaushofer,
684 K., Fratzl, P. 2005. Two different correlations between nanoindentation modulus and mineral
685 content in the bone–cartilage interface. J Struct Biol **149**, 138-148.
686 Guo, X.E. 2001. Mechanical properties of cortical bone and cancellous bone tissue. Ch. 10 in
687 *Bone Mechanics Handbook*, 2nd Ed. Cowin, S.C., Ed. Boca Raton (FL), CRC Press, pp 10-1-
688 10-23.
689 Hubbell, J.H., Seltzer, S.M. 2004. Tables of X-Ray Mass Attenuation Coefficients and Mass
690 Energy-Absorption Coefficients from 1 keV to 20 MeV for Elements $Z = 1$ to 92 and 48
691 Additional Substances of Dosimetric Interest. NISTIR 5632, accessed Aug. 7, 2020.
692 https://www.nist.gov/pml/x-ray-mass-attenuation-coefficients
693 Ingle, D.I., Natanson, L.J., Porter, M.E. 2018. Mechanical behavior of shark vertebral centra at
694 biologically relevant strains. J Exp Biol **221,** 188318.
695 Kinney, J. H., Haupt, D.L., Balooch, M., Ladd, A. J. C., Ryaby, J. T. , Lane, N. E. 2000. Three-
696 dimensional morphometry of the L6 vertebra in the ovariectomized rat model of
697 osteoporosis: Biomechanical implications. J Bone Miner Res **15**, 1981-1991.

698 Liu, X., Dean, M.N., Youssefpour, H., Summers, A.P., Earthamn, J.C. 2014. Stress relaxation
699 behavior of tesselated cartilage from the jaws of blue sharks. J Mech Behav Biomed Mater
700 **29**, 68-80.
701 Long, J.H. Jr., Koob, T., Schaefer, J., Summers, A., Bantilan, K., Grotmol, S. Porter, M. 2011.
702 Inspired by sharks: A biomimetic skeleton for the flapping, propulsive tail of an aquatic
703 robot. Marine Technol Soc J **45**(4), 119-129.
704 Malecki, A., Potdevin, G., Biernath,T., Eggl, E., Willer, K., Lasser, T., Maisenbacher, J.,
705 Gibmeier, J., Wanner, A., Pfeiffer, F. 2014. X-ray tensor tomography. Europhys Lett **105**,
706 38002.
707 Martins, R.V., Ohms, C., and Decroos, K. 2010. Full 3D spatially resolved mapping of residual
708 strain in a 316L austenitic stainless steel weld specimen. Mater Sci Eng A **527**, 4779–4787.
709 Morse, P.E., Stock, M.K., James, K.C., Natanson, L.J., Stock, S.R. 2022. Shark vertebral
710 microanatomy and mineral density variation studied with laboratory microComputed
711 Tomography. J Struct Biol **214**, 107831.
712 Naik, N.N., Jupe, A.C., Stock, S.R., Wilkinson, A.P., Lee, P.L., Kurtis, K.E. 2006. Sulfate attack
713 monitored by microCT and EDXRD: Influence of cement type, water-to-cement ratio, and
714 aggregate. Cement Concrete Res **36**, 144-159.
715 Natanson, L.J., Skomal, G.B., Hoffmann, S.L., Porter, M.E., Goldman, K.J., Serra, D. 2018. Age
716 and growth of sharks: do vertebral band pairs record age? Mar Freshwater Res **69**, 1440-
717 1452.
718 Niebur, G.L., Feldstein, M.J., Yuen, J.C., Chen, T.J., Keaveny, T.M. 2000. High-resolution finite
719 element models with tissue strength asymmetry accurately predict failure of trabecular bone.
720 J Biomech **33**, 1575-1583.

721 Park, J.S., Lienert, U., Dawson, P.R., and Miller, M.P. 2013. Quantifying Three-Dimensional
722 Residual Stress Distributions Using Spatially-Resolved Diffraction Measurements and Finite
723 Element Based Data Reduction. Exp Mech **53**, 1491–1507.
724 Park, J.-S. Almer, J.D., James, K.C., Natanson, L.J., Stock, S.R. 2022a. Mineral in shark
725 vertebrae studied by wide angle and by small angle x-ray scattering. Under revision.
726 Park, J.-S., Laugesen, M., Mays, S., Birkedal, H., Almer, J.D., Stock, S.R. 2022b. Intact
727 archeological human bones studied with transmission x-ray diffraction and small angle x-ray
728 scattering. Int J Osteoarchaeol **32**, 170-181.
729 Park, J.S., Chuang, A.C., Okasinski, J., Chen, H., Shade, P., Stock, S.R., Almer, J. A new
730 residual strain mapping program using energy dispersive x-ray diffraction at the Advanced
731 Photon Source. 2022c. Exp Mech, accepted.
732 Porter, M.E., Long, J.H. Jr. 2010. Vertebrae in compression: Mechanical behavior of arches and
733 centra in the gray smooth-hound shark (*Mustelus californicus*). J Morphol **271**, 366-375.
734 Porter, M.E., Diaz, C., Sturm, J.J., Grotmol, S., Summers, A.P., Long, J.H., Jr. 2014. Built for
735 speed: strain in the cartilaginous vertebral columns of sharks. Zool **117**, 19-27.
736 Porter, M.E., Ewoldt, R.H., Long, J.H. Jr. 2016. Automatic control: the vertebral column of
737 dogfish sharks behaves as a continuously variable transmission with smoothly shifting
738 functions. J Exp Biol **219**, 2908-2919.
739 Ryan, J., Stulajter, M.M., Okasinski, J.S., Cai, Z., Gonzalez, G.B., Stock, S.R. 2020. Carbonated
740 apatite lattice parameter variation across incremental growth lines in teeth. Materialia **14**,
741 100935.
742 Seidel, R., Roschger, A., Li, L., Bizzarro, J.J., Zhang, Q., Yin, J., Yang, T., Weaver, J.C., Fratzl,
743 P. Roschger, P., Dean, M.N. 2019. Mechanical properties of stingray tesserae: High-

744 resolution correlative analysis of mineral density and indentation moduli in tessellated
745 cartilage. Acta Biomater **96**, 421-435.
746 Seidel, R., Jayasankar, A.K., Dean, M.N. 2021. The multiscale architecture of tessellated
747 cartilage and its relation to function. J Fish Biol **98**, 942-955.
748 Stock, S.R. 2019. *MicroComputed Tomography: Methodology and Applications*, 2nd Ed., Taylor
749 and Francis.
750 Stock, S.R., DeCarlo, F., Almer, J.D. 2008. High energy x-ray scattering tomography applied to
751 bone. J Struct Biol **161**, 144-150.
752 Stock, S.R., Deymier-Black, A.C., Veis, A., Telser, A., Lux, E., Cai, Z. 2014. Bovine and equine
753 peritubular and intertubular dentin. Acta Biomater **10**, 3969-3977.
754 Stock, S.R., Yuan, Fang, Brinson, L.C., Almer, J.D. 2011. High-energy x-ray scattering
755 quantification of internal strains and their gradients in bone under load. J Biomech **44**, 291-
756 296.
757 Stock, S.R., Stock, M.K., Almer, J.D. 2020. Combined Computed Tomography and position-
758 resolved x-ray diffraction of an intact Roman-era Egyptian portrait mummy. J Royal Soc
759 Interface **17**, 20200686.
760 Stock, S.R., Park, J.-S., Jakus, A., Birkbak, M., Frølich, S., Birkedal, H., Shah, R., Almer, J.D.
761 2021. *"In situ* loading and x-ray diffraction quantification of strains in hydroxyapatite
762 particles within a 3D printed scaffold." Materialia **18**, 101174.
763 Stock, S.R., Morse, P.E., Stock, M.K., James, K.C., Natanson, L.J., Chen, Haiyan, Shevchenko,
764 P.D., Maxey, E.R., Antipova, O.A., Park, J.-S. 2022. "Microstructure and energy dispersive
765 diffraction reconstruction of 3D patterns of crystallographic texture in a shark centrum." J
766 Medical Imaging **9**, 031504.

767 Urist, M.R. 1961. Calcium and phosphorus in the blood and skeleton of the Elasmobranchii.
768 Endocrinol **69**, 778-801.
769 van Rietbergen, B. 2001. Micro-FE analyses of bone - State of the art. in Noninvasive
770 Assessment of Trabecular Bone Architecture and the Competence of Bone. Bay, B.K.,
771 Majumdar, S. Eds. New York, Kluwer/Plenum. **Adv Exp Med Biol Vol 496:** 21-30.
772 Watanabe, Y.Y., Lydersen, C., Fisk, A.T., Kovacs, K.M. 2012. The slowest fish: Swim speed
773 and tail-beat frequency of Greenland sharks. J Exp Mar Biol Ecol **426/427**, 5-11.
774 Weidner, D.J., Vaughan, M.T., Wang, L., Long, H., Li, L., Dixon, N.A., Durham, W.B. 2010.
775 Precise stress measurements with white synchrotron x-rays. Rev Sci Instrum **81**, 013903.
776
777 **Figure captions**

778 Fig. 1. Schematics of sharks. (a) Side view of a generalized shark. The blocks within the
779 silhouette represent the vertebrae: gray for cervical and thoracic vertebrae and black for
780 abdominal vertebrae. The arrow indicates very approximately the position of the vertebrae in this
781 study. (b) Schematic from above of vertebral compression when a shark swims, illustrated
782 schematically by three positions of the tail. When the tail swings to the right (right tail diagram),
783 the right side of the vertebra is compressed (right trapezoid with arrows indicating compression).
784 As the left side of the schematic indicates, the vertebra's opposite (left) side compresses when
785 the tail moves to the left. Panels (c) and (d) show lamniform (left column) and carcharhiniform
786 (right column) abdominal centra. (c) 3D representation of a lamniform and a carcharhiniform
787 centrum with some material shown transparent so that the structures' cross-sections can be seen.
788 c - hourglass-shaped cone walls, i – intermedialia, L – lamella, W – wedge. (d) Thresholded
789 slices (black in these transverse sections perpendicular to the vertebral column axis and near the
790 centra's axial midplane) of a mako centrum (lamniform shark mapped in this study) showing the

791 radial lamellae and of a sandbar shark centrum (carcharhiniform shark similar to the blue shark
792 mapped in this study). The dorsal-ventral plane is vertical (double arrowed line), and the
793 intersection of the frontal (coronal) plane with each slice is shown as a horizontal red dotted line.
794 Gaps "g" between wedges (sandbar shark) and between groups of closely spaced lamellae (mako
795 shark) are labeled.

796 Fig. 2. Schematic of the EDD apparatus with the arrangement of ten detector elements and of
797 the sampling scheme illustrated for a lamniform and a carcharhiniform shark. (a) Energy
798 dispersive diffraction apparatus illustrated with a schematic of a lamniform centrum. A set of
799 three orthogonal linear translators (along X, Y and Z) scan the specimen across the sampling
800 volume "sv". The other main components are: detector elements "de", conical slits "cs" and
801 incident beam collimator "col". (b) Arrangement of detector elements 1-10 and the orientation of
802 different lattice plane normals $\mathbf{N}_1$ and $\mathbf{N}_5$ for the crystallites producing diffracted intensities
803 measured in detectors 1 and 5. (c) Schematic of shortfin mako and (d) diagram of blue shark
804 sampling grids illustrated by side views (top) and transverse views (bottom) of the two centra.
805 The labels are: cone wall "cw", lamellae "L", wedge "W" and vertebral column axis "vca". Note
806 that only a small portion of the shortfin mako centrum was covered, but the entire volume of the
807 blue shark centrum was scanned.

808 Fig. 3. Typical energy dispersive diffraction pattern from a shark centrum. The 00.2 and "q"
809 (unresolved 21.1, 11.2, 30.0 and 20.2) peaks from hAp are labeled as well as peaks "cal" from
810 the calibration source. The green peaks below the data are for a synthetic hAp reference pattern
811 (Powder Diffraction File 86-1201).

812 Fig. 4. Orthogonal sections through the blue shark centrum reconstructed with the integrated
813 intensity of the quadruplet reflection (21.1+11.2+30.0+20.2). The brighter the pixel, the higher

814 the intensity in the voxel. The number in the upper left of each panel identifies the detector
815 number. The gray scale images of the top row show intensities recorded with detector 5 (left) and
816 the diametrically opposite detector 10 (middle) and of the bottom row intensities from detectors
817 1 (left) and diametrically opposite 9 (right). The color panels (right column) show the combined
818 intensities of detectors 5 and 10 (top) and 1 and 9 (bottom) with 5 and 9 in blue and 10 and 1 in
819 red. The yellow arrowheads identify the cone wall diffracting greater intensity than the adjacent
820 intermedialia. The orange arrowheads show portions of the maps where intermedialia and cone
821 wall intensities are comparable. The yellow (and one black) boxes in the detector 5 and 1 panels
822 indicate the positions of 3 voxel x 3 voxel x 1 voxel regions used to measure mean diffracted
823 intensity within the cone wall (*cw*) and intermedialia (*i, i'*); these values are reported in Table 2.
824 Fig. 5. (a) Orthogonal sections through the blue shark centrum reconstructed with the 00.2
825 integrated intensity. The brighter the pixel, the higher the intensity in the voxel. Intensities from
826 detectors 5 (blue), 7 (green) and 9 (red) are combined. The different colored arrows show the *c*-
827 axis orientation measured by each detector. (b) Schematic of the bioapatite *c*-axis orientations
828 revealed in panel a. The white boxes indicate the positions of 3 voxel x 3 voxel x 1 voxel regions
829 used to measure mean diffracted intensity within the cone wall (*cw*), intermedialia (*i, i'*) and
830 fluid (*f*) for detectors 1 and 5; these values are reported in Table 2.
831 Fig. 6. Shortfin mako's spatial distribution of diffracted intensity measured with the ten
832 detectors for the quadruplet q (a) and 00.2 (b) reflections. The color bar between the panels gives
833 the intensity range which was 0 to 1,200 a.u. for q and 0-150 for 00.2. The detector data are
834 placed in their correct relative orientations. The transverse section is from near the centrum's
835 axial center and covers only part of the cross-section. Portions of two gaps (g1 and g2) and of
836 three sectors (s1, s2 and s3) are labeled in the detector 1 map of (a) as is the 2 mm scale bar

837 (white bar at the bottom). The segmented image inset in the middle of (a) is a lab microCT slice
838 of the same centrum (from Morse et al. 2022).
839 Fig. 7. Illustration of how carcharhiniform centra data could be incorporated into
840 numerical models of mechanical response to loading. Centra 3D macroarchitecture from lab
841 microCT (e.g. Morse et al. 2022) would be converted into a 3D model of the structure.
842 Incompressible intervertebral fluid (ivf) would fill the space between the cones and the rigid
843 platens applying load P. (a) Simple uniaxial compression of centra simplified to contain two
844 isotropic phases: mineralized cartilage (mc, dark gray) and unmineralized cartilage (uc, light
845 gray). The magenta arrows (xs) mark the position of the cross-section shown at the bottom of the
846 panel. The centrum geometry is defined by diameter ϕ, height h and hourglass angle α. (b)
847 Distribution of loads for simulated bending. The location of two large and two small wedges
848 beneath the cone are shown in yellow, and the largest load occurs at the center of the outer edge
849 of the large wedges, mimicking in vivo bending. Here the wedge and cone materials are not
850 differentiated. (c) Non-uniform loading and partition of the mineralized cartilage into cone “c”
851 (with thickness δ, shown in black) and intermedialia “i” (bottom panel). The corresponding 3D
852 model (top panel) includes unmineralized cartilage “uc”, the intermedialia is in the form of
853 wedges "W" and isotropic Young’s moduli $E_c > E_W >> E_{uc}$. (d) Transverse centrum cross-section
854 at the axial position between the cone apex and its axial end. The radial *r*, tangential *t* and axial *a*
855 directions are indicated as are the potentially differing Young’s moduli along these three
856 directions. The text at the bottom of the panel indicates expected relative magnitudes of moduli
857 along different directions for the wedge and cone; this is based on the *c*-axis crystallographic
858 textures reported in this paper.
859

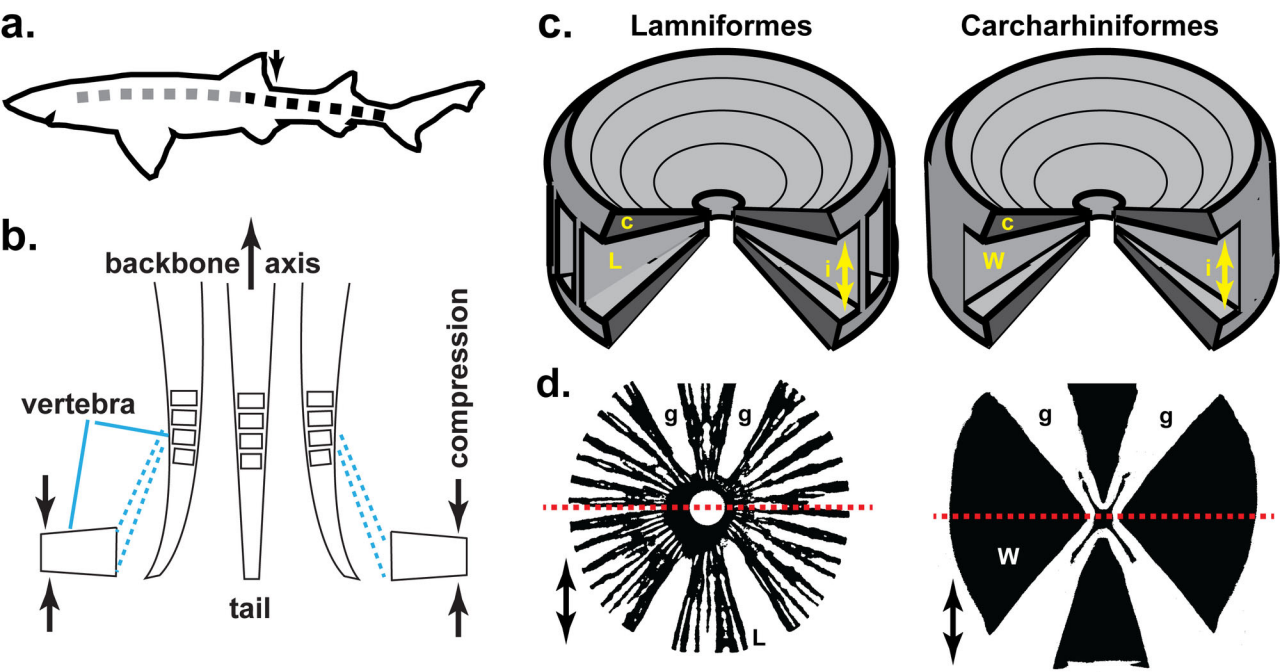
a.
b.
backbone axis
vertebra
compression
tail
c.
Lamniformes
Carcharhiniformes
c
L
i
c
W
i
d.
g
g
L
g
g
W

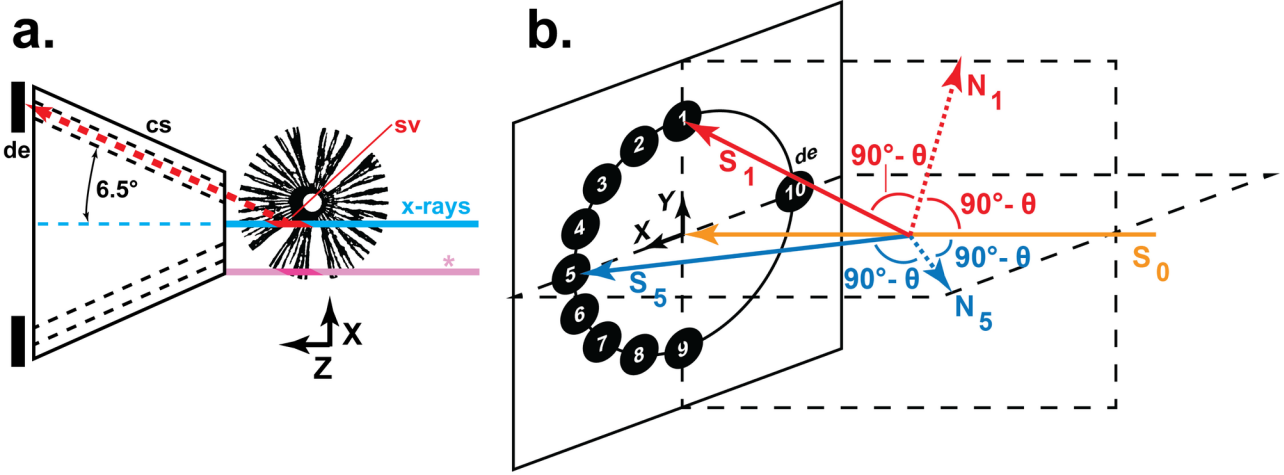
a.
b.
de
cs
sv
6.5°
x-rays
*
X
Z
1
2
3
4
5
6
7
8
9
10
de
S 1
S 5
S 0
N 1
N 5
Y
X
90°- θ
90°- θ
90°- θ
90°- θ

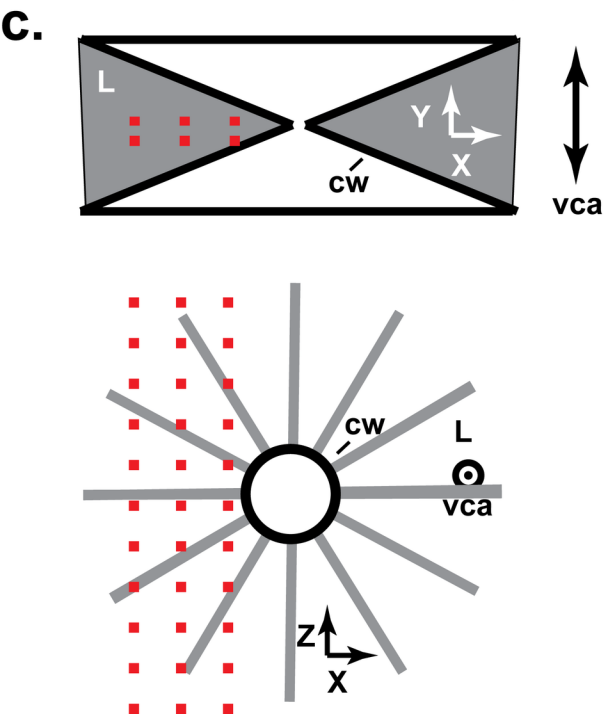
c.
L
Y
X
cw
vca
cw
L
vca
Z
X

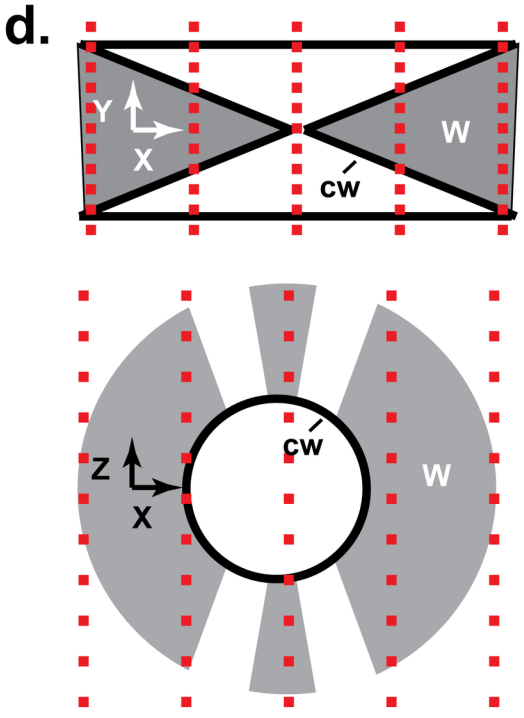
d.
Y
X
cw
W
cw
Z
X
W

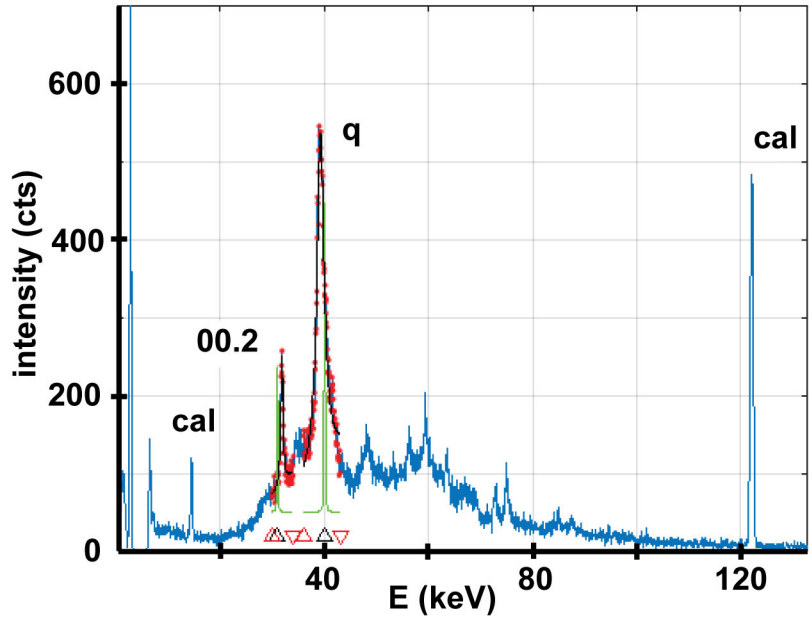
600
400
200
0
intensity (cts)
q
cal
00.2
cal
40
80
120
E (keV)

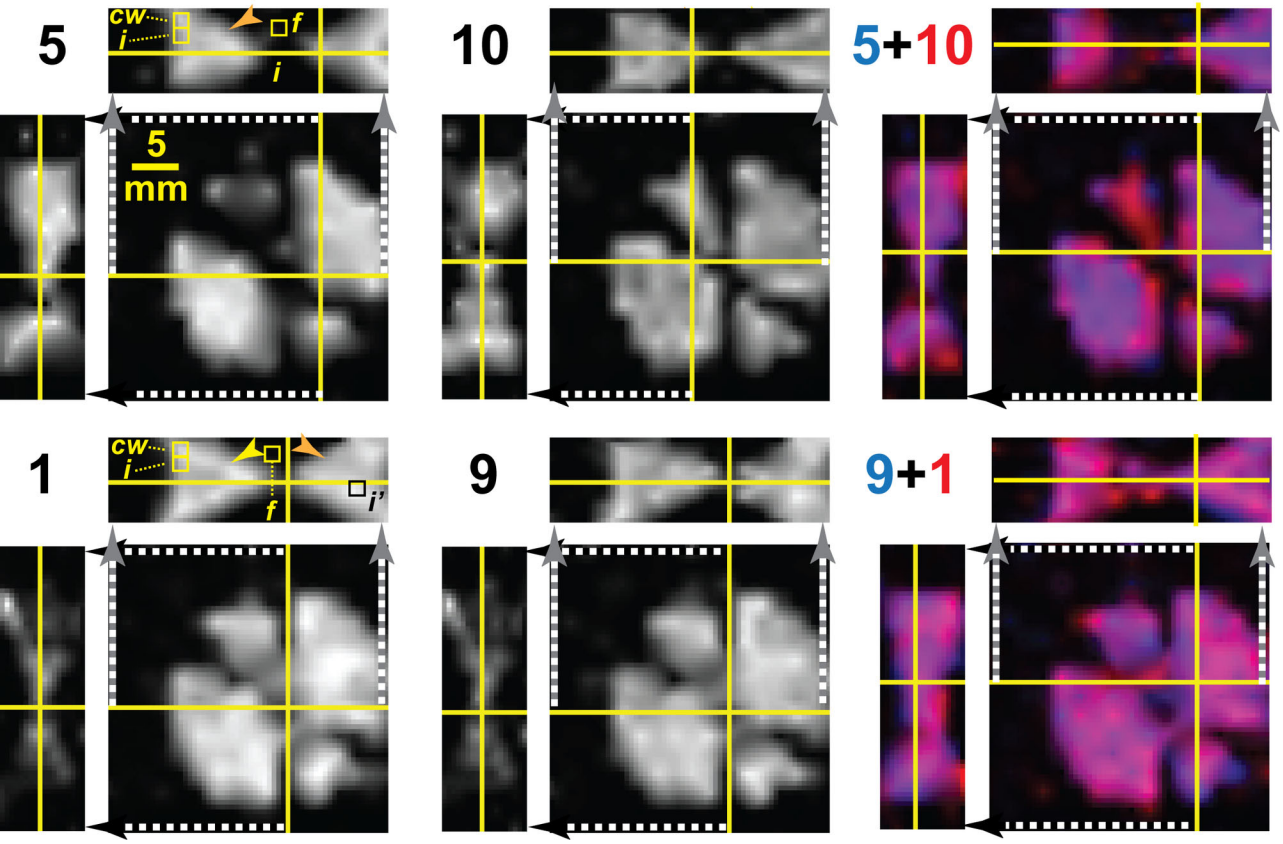
5
cw
i
f
i
5
mm
10
5+10
1
cw
i
f
i'
9
9+1

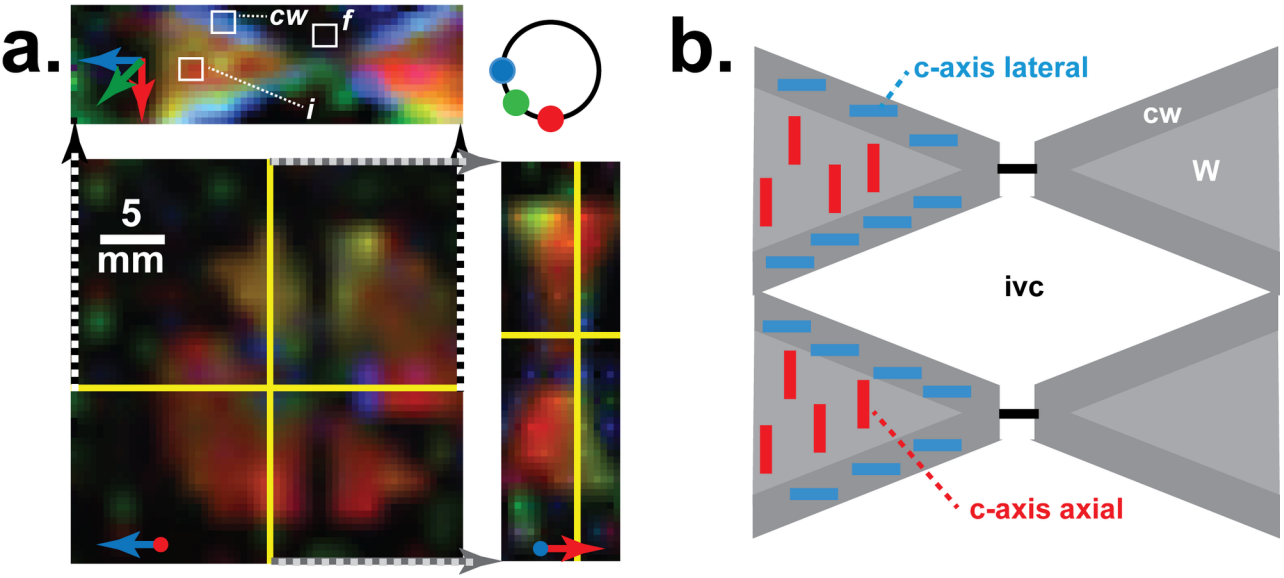
a.
cw
f
i
5
mm
b.
c-axis lateral
cw
W
ivc
c-axis axial

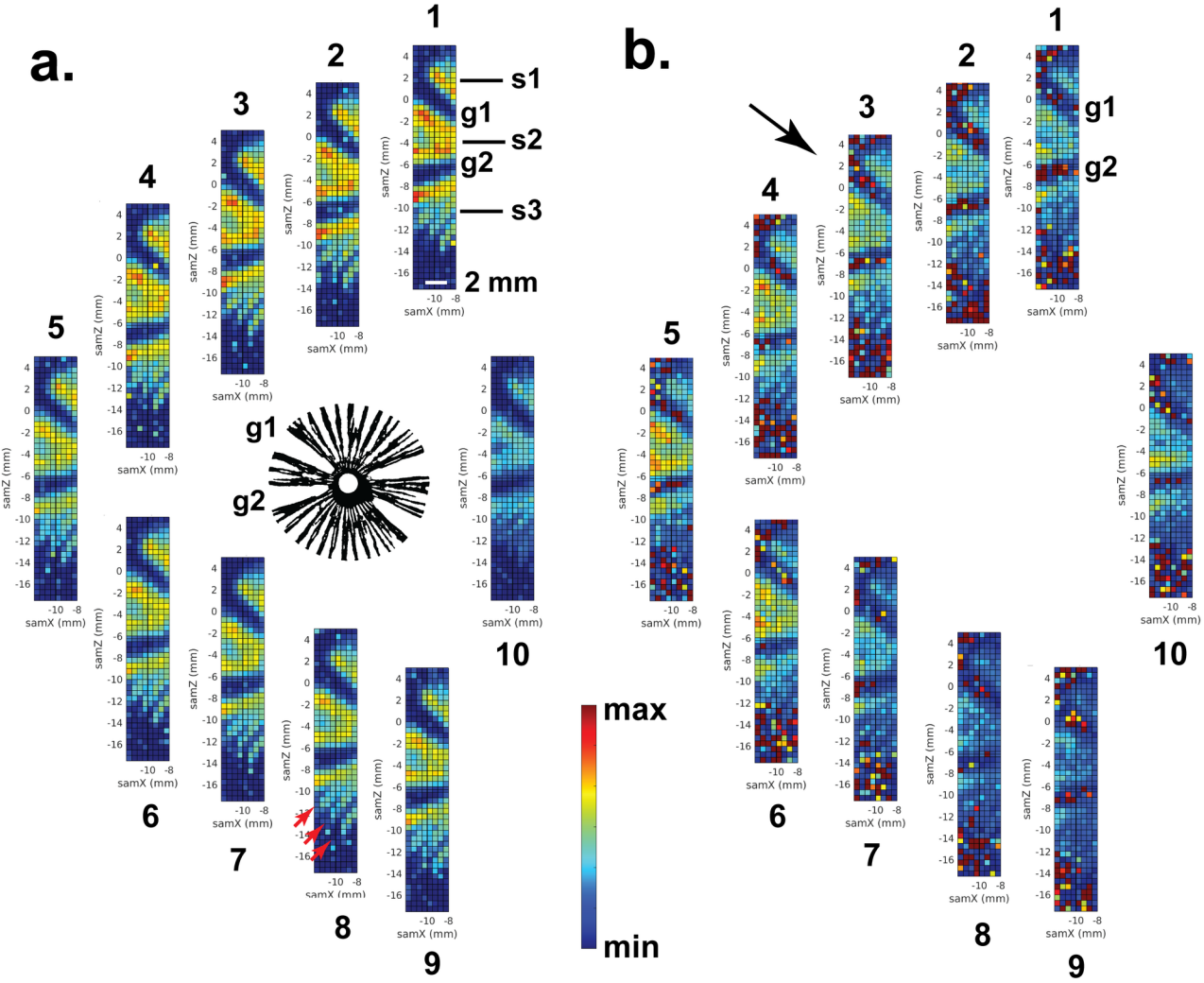
a.
b.
1
2
3
4
5
6
7
8
9
10
s1
g1
s2
g2
s3
2 mm
max
min
samZ (mm)
samX (mm)

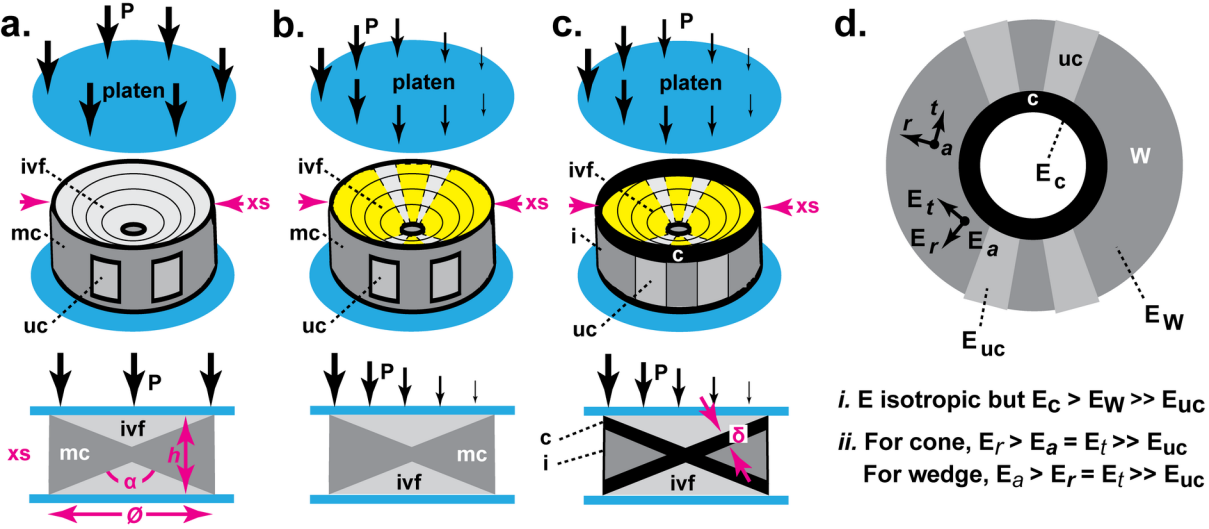

i. E isotropic but $E_c > E_W >> E_{uc}$

ii. For cone, $E_r > E_a = E_t >> E_{uc}$
For wedge, $E_a > E_r = E_t >> E_{uc}$

Table 1. Experimental parameters

	Gage volume (mm)			Step size (mm)			Number of steps			exposure
Shark	δX	δY	δZ	ΔX	ΔY	ΔZ	N_X	N_Y	N_Z	(s)
Mako	0.2	0.2	2.5	1.5	0.5	1.0	3	10	47	50
Blue	0.1	0.2	1.7	2.0	1.0	1.9	16	10	17	30

Table 2. Integrated intensities in the cone wall (cw) and intermedialia (i) of the q and 00.2 reflections for the blue shark centrum. Mean values are for the 3 voxel x 3 voxel regions within the yellow squares of Fig. 4 and Fig. 5. The standard deviation of each mean is the number following ±. The maximum integrated intensity of the 3D reconstructed volume with q reflection was 98 (arbitrary units) and with the 00.2 reflection was 86 (arbitrary units, a.u.). For 00.2, the integrated intensity recorded within fluid-filled volumes were 2 a.u. for detectors 1 and 5, and, for q, values were 2 and 4 a.u., respectively.

Reflection	detector 5		detector 1		
	cw	*i*	*cw*	*i*	*i'*
q	68 ± 7	61 ± 9	66 ± 7	46 ± 10	72 ± 3
00.2	46 ± 9	5 ± 1	21 ± 5	35 ± 2	

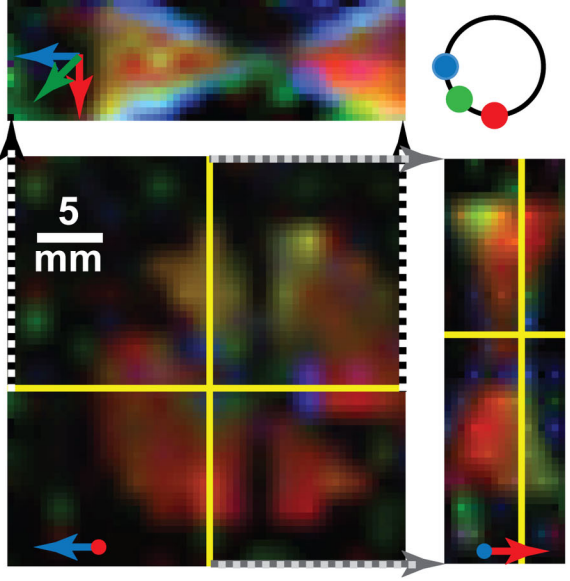

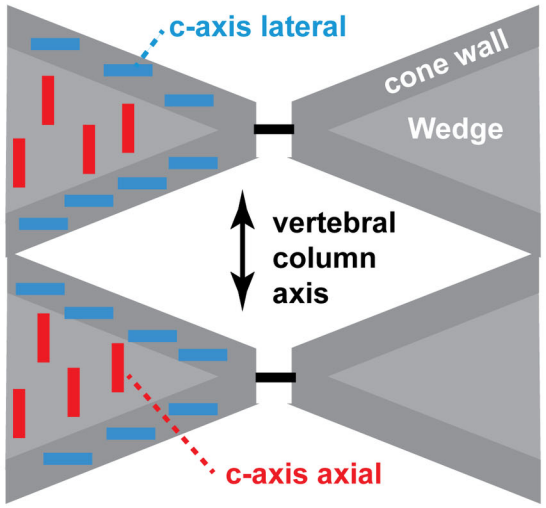

Bioapatite crystal orientations in blue shark centrum. (left) Energy dispersive diffracted intensity in 3D (colors indicate intensity along different anatomical directions). (right) Schematic indicating crystal c-axes in different portions of the centrum.